Author(s): Tuovinen, Toni & Awan, Hafiz Asad Ali & Saarakkala, Seppo E. & Hinkkanen, Marko

Title: Discrete-time observer design for sensorless synchronous motor drives

Year: 2015

Version: Post print

Please cite the original version:

Tuovinen, Toni & Awan, Hafiz Asad Ali & Saarakkala, Seppo E. & Hinkkanen, Marko. 2015. Discrete-time observer design for sensorless synchronous motor drives. IEEE Energy Conversion Congress and Exposition (ECCE). 867-874. ISBN 978-1-4673-7150-6 (electronic). DOI: 10.1109/ecce.2015.7309779.

Discrete-Time Observer Design for Sensorless Synchronous Motor Drives

Toni Tuovinen*, Hafiz Asad Ali Awan†, Seppo E. Saarakkala†, and Marko Hinkkanen†
*ABB Drives, Helsinki, Finland
†Aalto University, Espoo, Finland

***Abstract*—This paper deals with the speed and position estimation of interior permanent-magnet synchronous motor (IPMSM) and synchronous reluctance motor (SyRM) drives. A speed-adaptive full-order observer is designed and analyzed in the discrete-time domain. The observer design is based on the exact discrete-time motor model, which inherently takes the delays in the control system into account. The proposed observer is experimentally evaluated using a 6.7-kW SyRM drive. The analysis and experimental results indicate that drastic performance improvements can be obtained with the direct discrete-time design, especially if the sampling frequency is relatively low compared to the fundamental frequency.**

***Index Terms*—Observer, parameter uncertainties, speed sensorless, stability conditions.**

I. Introduction

Synchronous motors with a magnetically anisotropic rotor—such as the interior permanent-magnet synchronous motor (IPMSM) and the synchronous reluctance motor (SyRM)—are becoming competitors to the induction motor in hybrid (or electric) vehicles [1], heavy-duty working machines, and industrial applications. In these applications, the maximum speeds and, consequently, the maximum operating frequencies can be very high, while the switching frequency is limited. Hence, the resulting ratio between the switching (sampling) frequency and the maximum fundamental frequency can be even below ten.

Motion-sensorless operation is commonly preferred [2]–[16]. Usually, a speed and position observer is first designed in the continuous-time domain and then discretized for the digital processor by means of the forward Euler, symplectic Euler, or Tustin approximations. A drawback of this approach is that the sampling frequency has to be at least 10–20 times higher than the desired maximum fundamental frequency.

Higher fundamental frequencies and improved robustness at a given sampling frequency can be achieved by designing the control system directly in the discrete-time domain [16]–[22]. For the direct discrete-time control design, a hold-equivalent discrete model—including the effects of the zero-order hold (ZOH) and sampler—of the motor drive is needed. The exact closed-form model for surface permanent-magnet synchronous motor (SPMSM) drives can be found in [17], [18]. For the IPMSM drives, an approximate discrete model has been proposed in [19], [20] and the exact closed-form model has been recently published in [22].

A continuous-time gain design [14] for a speed-adaptive full-order observer guarantees the local stability of the estimation-error dynamics at every operating point (except at zero speed) in ideal conditions. However, the effects of the digital implementation were not considered. If the ratio between the sampling frequency and the fundamental frequency is low, the stability conditions derived in [14] are not valid and the system can even become unstable.

In this paper, a speed-adaptive full-order observer for sensorless IPMSM and SyRM drives is designed directly in the discrete-time domain. First, the motor model and the observer design in the continuous-time domain are reviewed in Section II. Then, the main contributions of the paper are presented in Section III:

- A linearized model for the discrete-time estimation-error dynamics is derived.
- A stabilizing observer gain is proposed based on the linearized model. The proposed design decouples the speed-estimation dynamics from the flux-estimation dynamics, which simplifies the observer tuning procedure.

Section IV describes an example design. In Section V, the proposed discrete-time observer design is evaluated by means of simulations and experiments using a 6.7-kW SyRM drive. Furthermore, the discrete-time design is compared to its continuous-time counterpart, which is discretized using the forward Euler approximation.

II. Review: Continuous-Time Model and Observer

Real space vectors will be used. For example, the stator-current vector is $\boldsymbol{i}_\mathrm{s} = [i_\mathrm{d}, i_\mathrm{q}]^\mathrm{T}$, where i_d and i_q are the components of the vector. The identity matrix is $\mathbf{I} = \left[\begin{smallmatrix}1 & 0\\ 0 & 1\end{smallmatrix}\right]$ and the orthogonal rotation matrix is $\mathbf{J} = \left[\begin{smallmatrix}0 & -1\\ 1 & 0\end{smallmatrix}\right]$. Vectors are denoted using boldface lowercase letters and matrices using boldface uppercase letters. Space vectors in stator and rotor coordinates are marked with the superscripts s and r, respectively. No superscript is used for space vectors in estimated rotor coordinates.

A. Model

The electrical rotor angle is denoted by ϑ_m and the electrical angular rotor speed is $\omega_\mathrm{m} = \mathrm{d}\vartheta_\mathrm{m}/\mathrm{d}t$. In rotor coordinates, the state-space representation corresponding to the standard model of the IPMSM is

$$\frac{\mathrm{d}\boldsymbol{\psi}_\mathrm{s}^\mathrm{r}(t)}{\mathrm{d}t} = \boldsymbol{A}(t)\boldsymbol{\psi}_\mathrm{s}^\mathrm{r}(t) + \boldsymbol{B}\boldsymbol{u}_\mathrm{s}^\mathrm{r}(t) + \boldsymbol{b}\psi_\mathrm{pm} \tag{1a}$$

$$\boldsymbol{i}_\mathrm{s}^\mathrm{r}(t) = \boldsymbol{C}\boldsymbol{\psi}_\mathrm{s}^\mathrm{r}(t) + \boldsymbol{d}\psi_\mathrm{pm} \tag{1b}$$

where $\boldsymbol{\psi}_\mathrm{s}$ is the stator flux vector, $\boldsymbol{u}_\mathrm{s}$ is the stator voltage vector, and ψ_pm is the permanent-magnet (PM) flux. The system matrices are

$$\boldsymbol{A}(t) = \begin{bmatrix} -R_\mathrm{s}/L_\mathrm{d} & \omega_\mathrm{m}(t) \\ -\omega_\mathrm{m}(t) & -R_\mathrm{s}/L_\mathrm{q} \end{bmatrix}, \quad \boldsymbol{B} = \mathbf{I}, \quad \boldsymbol{b} = \begin{bmatrix} R_\mathrm{s}/L_\mathrm{d} \\ 0 \end{bmatrix}$$
$$\boldsymbol{C} = \begin{bmatrix} 1/L_\mathrm{d} & 0 \\ 0 & 1/L_\mathrm{q} \end{bmatrix}, \quad \boldsymbol{d} = \begin{bmatrix} -1/L_\mathrm{d} \\ 0 \end{bmatrix} \tag{2}$$

where R_s is the stator resistance, L_d is the direct-axis inductance, and L_q is the quadrature-axis inductance. The state-space representation in (1) has two inputs: the stator voltage $\boldsymbol{u}_\mathrm{s}$ and the PM flux ψ_pm (which is constant). If $L_\mathrm{d} = L_\mathrm{q}$, the model represents the SPMSM. If $\psi_\mathrm{pm} = 0$, the model of the SyRM is obtained. In the following equations, the time dependency is not explicitly written in order to simplify the notation.

B. Observer Structure

The speed-adaptive full-order observer in estimated rotor coordinates is defined by [8], [14]

$$\frac{\mathrm{d}\hat{\boldsymbol{\psi}}_\mathrm{s}}{\mathrm{d}t} = \hat{\boldsymbol{A}}\hat{\boldsymbol{\psi}}_\mathrm{s} + \boldsymbol{B}\boldsymbol{u}_\mathrm{s} + \boldsymbol{b}\psi_\mathrm{pm} + \boldsymbol{K}_\mathrm{c}\tilde{\boldsymbol{i}}_\mathrm{s} \tag{3a}$$
$$\hat{\boldsymbol{i}}_\mathrm{s} = \boldsymbol{C}\hat{\boldsymbol{\psi}}_\mathrm{s} + \boldsymbol{d}\psi_\mathrm{pm} \tag{3b}$$

where the estimates are marked by the hat, $\tilde{\boldsymbol{i}}_\mathrm{s} = \hat{\boldsymbol{i}}_\mathrm{s} - \boldsymbol{i}_\mathrm{s}$ is the estimation error of the stator current, and $\boldsymbol{K}_\mathrm{c}$ is a 2×2 gain matrix. Further, the motor parameter estimates are assumed to be accurate in order to simplify the notation. The electrical rotor angle is estimated using

$$\frac{\mathrm{d}\hat{\vartheta}_\mathrm{m}}{\mathrm{d}t} = \hat{\omega}_\mathrm{m} \tag{4}$$

The proportional-integral (PI) speed-adaptation law is

$$\frac{\mathrm{d}\hat{\omega}_\mathrm{i}}{\mathrm{d}t} = \boldsymbol{k}_\mathrm{ic}\tilde{\boldsymbol{i}}_\mathrm{s}, \quad \hat{\omega}_\mathrm{m} = \hat{\omega}_\mathrm{i} + \boldsymbol{k}_\mathrm{pc}\tilde{\boldsymbol{i}}_\mathrm{s} \tag{5}$$

where $\hat{\omega}_\mathrm{i}$ is the integral state. The gain vectors are $\boldsymbol{k}_\mathrm{ic} = [0, k_\mathrm{ic}]$ and $\boldsymbol{k}_\mathrm{pc} = [0, k_\mathrm{pc}]$, i.e., only the estimation error in the estimated q-axis direction is used for speed estimation. It is worth noticing that the matrix $\hat{\boldsymbol{A}}$ in (3) depends on the estimated speed $\hat{\omega}_\mathrm{m}$.

C. Estimation-Error Dynamics

1) Nonlinear Dynamics: For analyzing the estimation-error dynamics, the plant model (1) is first transformed to estimated rotor coordinates as

$$\frac{\mathrm{d}\boldsymbol{\psi}_\mathrm{s}}{\mathrm{d}t} = \boldsymbol{A}'\boldsymbol{\psi}_\mathrm{s} + \boldsymbol{B}\boldsymbol{u}_\mathrm{s} + \boldsymbol{b}'\psi_\mathrm{pm} \tag{6a}$$
$$\boldsymbol{i}_\mathrm{s} = \boldsymbol{C}'\boldsymbol{\psi}_\mathrm{s} + \boldsymbol{d}'\psi_\mathrm{pm} \tag{6b}$$

where $\boldsymbol{\psi}_\mathrm{s} = \mathrm{e}^{-\tilde{\vartheta}_\mathrm{m}\mathbf{J}}\boldsymbol{\psi}_\mathrm{s}^\mathrm{r}$ and $\tilde{\vartheta}_\mathrm{m} = \hat{\vartheta}_\mathrm{m} - \vartheta_\mathrm{m}$. Other space vectors are transformed similarly. The matrices become

$$\boldsymbol{A}' = \mathrm{e}^{-\tilde{\vartheta}_\mathrm{m}\mathbf{J}}\boldsymbol{A}\mathrm{e}^{\tilde{\vartheta}_\mathrm{m}\mathbf{J}} - \tilde{\omega}_\mathrm{m}\mathbf{J}, \quad \boldsymbol{b}' = \mathrm{e}^{-\tilde{\vartheta}_\mathrm{m}\mathbf{J}}\boldsymbol{b}$$
$$\boldsymbol{C}' = \mathrm{e}^{-\tilde{\vartheta}_\mathrm{m}\mathbf{J}}\boldsymbol{C}\mathrm{e}^{\tilde{\vartheta}_\mathrm{m}\mathbf{J}}, \quad \boldsymbol{d}' = \mathrm{e}^{-\tilde{\vartheta}_\mathrm{m}\mathbf{J}}\boldsymbol{d} \tag{7}$$

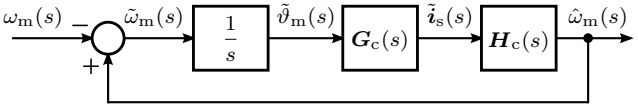

Fig. 1. Linearized estimation-error dynamics for the continuous-time observer design.

The estimation error of the stator flux is $\tilde{\boldsymbol{\psi}}_\mathrm{s} = \hat{\boldsymbol{\psi}}_\mathrm{s} - \boldsymbol{\psi}_\mathrm{s}$ and the estimation errors of other variables are defined similarly. The nonlinear estimation-error dynamics are

$$\frac{\mathrm{d}\tilde{\boldsymbol{\psi}}_\mathrm{s}}{\mathrm{d}t} = (\hat{\boldsymbol{A}} + \boldsymbol{K}_\mathrm{c}\boldsymbol{C})\tilde{\boldsymbol{\psi}}_\mathrm{s} + (\tilde{\boldsymbol{A}} + \boldsymbol{K}_\mathrm{c}\tilde{\boldsymbol{C}})\boldsymbol{\psi}_\mathrm{s} + (\tilde{\boldsymbol{b}} + \boldsymbol{K}_\mathrm{c}\tilde{\boldsymbol{d}})\psi_\mathrm{pm} \tag{8a}$$
$$\tilde{\boldsymbol{i}}_\mathrm{s} = \boldsymbol{C}\tilde{\boldsymbol{\psi}}_\mathrm{s} + \tilde{\boldsymbol{d}}\psi_\mathrm{pm} + \tilde{\boldsymbol{C}}\boldsymbol{\psi}_\mathrm{s} \tag{8b}$$

where $\tilde{\boldsymbol{A}} = \hat{\boldsymbol{A}} - \boldsymbol{A}'$, $\tilde{\boldsymbol{b}} = \boldsymbol{b} - \boldsymbol{b}'$, $\tilde{\boldsymbol{C}} = \boldsymbol{C} - \boldsymbol{C}'$, and $\tilde{\boldsymbol{d}} = \boldsymbol{d} - \boldsymbol{d}'$.

2) Linearized Dynamics: The nonlinear dynamics in (8) can be linearized for analysis purposes, leading to [9]

$$\frac{\mathrm{d}\tilde{\boldsymbol{\psi}}_\mathrm{s}}{\mathrm{d}t} = \boldsymbol{A}_{\psi\mathrm{c}}\tilde{\boldsymbol{\psi}}_\mathrm{s} + \boldsymbol{b}_{\vartheta\mathrm{c}}\tilde{\vartheta}_\mathrm{m} \tag{9a}$$
$$\tilde{\boldsymbol{i}}_\mathrm{s} = \boldsymbol{C}\tilde{\boldsymbol{\psi}}_\mathrm{s} + \boldsymbol{d}_{\vartheta\mathrm{c}}\tilde{\vartheta}_\mathrm{m} \tag{9b}$$

The system matrices are

$$\boldsymbol{A}_{\psi\mathrm{c}} = \boldsymbol{A}_0 + \boldsymbol{K}_\mathrm{c}\boldsymbol{C}, \quad \boldsymbol{d}_{\vartheta\mathrm{c}} = (\mathbf{J}\boldsymbol{C} - \boldsymbol{C}\mathbf{J})\,\boldsymbol{\psi}_{\mathrm{s}0} + \mathbf{J}\boldsymbol{d}\psi_\mathrm{pm}$$
$$\boldsymbol{b}_{\vartheta\mathrm{c}} = (\boldsymbol{A}_{\psi\mathrm{c}} + \omega_{\mathrm{m}0}\mathbf{J})\boldsymbol{C}^{-1}\boldsymbol{d}_{\vartheta\mathrm{c}} \tag{10}$$

where the operating-point quantities are marked with the subscript 0. The system (9) can be represented by the transfer-function matrix

$$\boldsymbol{G}_\mathrm{c}(s) = \boldsymbol{C}(s\mathbf{I} - \boldsymbol{A}_{\psi\mathrm{c}})^{-1}\boldsymbol{b}_{\vartheta\mathrm{c}} + \boldsymbol{d}_{\vartheta\mathrm{c}} \tag{11}$$

from $\tilde{\vartheta}_\mathrm{m}(s)$ to $\tilde{\boldsymbol{i}}_\mathrm{s}(s)$. Further, the speed-adaptation law (5) corresponds to the transfer-function matrix $\boldsymbol{H}_\mathrm{c}(s) = \boldsymbol{k}_\mathrm{pc} + \boldsymbol{k}_\mathrm{ic}/s$ from $\tilde{\boldsymbol{i}}_\mathrm{s}(s)$ to $\hat{\omega}_\mathrm{m}(s)$. Fig. 1 shows the block diagram of the linearized estimation-error dynamics. The closed-loop transfer function from the actual speed to the estimated speed is

$$\frac{\hat{\omega}_\mathrm{m}(s)}{\omega_\mathrm{m}(s)} = \frac{\boldsymbol{H}_\mathrm{c}(s)\boldsymbol{G}_\mathrm{c}(s)}{s + \boldsymbol{H}_\mathrm{c}(s)\boldsymbol{G}_\mathrm{c}(s)} \tag{12}$$

D. Gain Selection

First, to simplify the notation in the following, an auxiliary variable

$$\beta = (L_\mathrm{d} - L_\mathrm{q})\frac{i_\mathrm{q}}{\psi_\mathrm{f}} \tag{13}$$

is defined, where the denominator $\psi_\mathrm{f} = \psi_\mathrm{pm} + (L_\mathrm{d} - L_\mathrm{q})i_\mathrm{d}$ can be interpreted as a fictitious flux [5], [13]. As special cases, $\beta = 0$ holds for SPMSMs and $\beta = i_\mathrm{q}/i_\mathrm{d}$ for SyRMs.

The fourth-order system shown in Fig. 1 is complicated and the gains can be difficult to tune. In order to simplify the tuning procedure, the speed-estimation dynamics and the flux-estimation dynamics can be decoupled by zeroing $\boldsymbol{b}_{\vartheta\mathrm{c}}$,

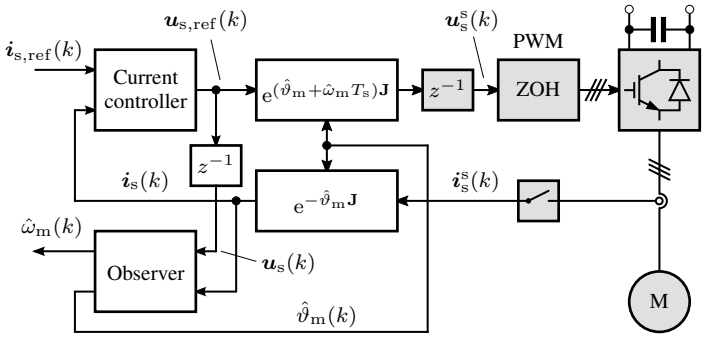

Fig. 2. Sensorless control system. The discrete-time plant model includes the grey blocks: motor, ZOH, and computational time delay z^{-1}. The white blocks represent the discrete-time control algorithm.

leading to $\boldsymbol{G}_{\mathrm{c}}(s) = \boldsymbol{d}_{\vartheta\mathrm{c}}$. From (10), the observer gain yielding $\boldsymbol{b}_{\vartheta\mathrm{c}} = \boldsymbol{0}$ can be solved as [14]

$$\boldsymbol{K}_{\mathrm{c}} = \begin{bmatrix} R_{\mathrm{s}} + L_{\mathrm{d}}k_{1\mathrm{c}} & -\beta L_{\mathrm{q}}k_{1\mathrm{c}} \\ L_{\mathrm{d}}k_{2\mathrm{c}} & R_{\mathrm{s}} - \beta L_{\mathrm{q}}k_{2\mathrm{c}} \end{bmatrix} \tag{14}$$

where

$$k_{1\mathrm{c}} = -\frac{b_{\mathrm{c}} + \beta(c_{\mathrm{c}}/\hat{\omega}_{\mathrm{m}} - \hat{\omega}_{\mathrm{m}})}{\beta^2 + 1}, \quad k_{2\mathrm{c}} = \frac{\beta b_{\mathrm{c}} - c_{\mathrm{c}}/\hat{\omega}_{\mathrm{m}} + \hat{\omega}_{\mathrm{m}}}{\beta^2 + 1} \tag{15}$$

The speed-adaptation gains are $k_{\mathrm{pc}} = L_{\mathrm{q}}d_{\mathrm{c}}/\psi_{\mathrm{f}}$ and $k_{\mathrm{ic}} = L_{\mathrm{q}}e_{\mathrm{c}}/\psi_{\mathrm{f}}$. With this gain selection, the characteristic polynomial of the estimation-error dynamics becomes $(s^2 + b_{\mathrm{c}}s + c_{\mathrm{c}})(s^2 + d_{\mathrm{c}}s + e_{\mathrm{c}})$, where the design parameters are $b_{\mathrm{c}} > 0$, $c_{\mathrm{c}} > 0$, $d_{\mathrm{c}} > 0$, and $e_{\mathrm{c}} > 0$, which may depend on the operating point. The design parameters b_{c} and c_{c} determine the flux-estimation error dynamics and the design parameters d_{c} and e_{c} determine the speed-adaptation dynamics. The resulting closed-loop transfer function from the actual speed to the estimated speed is

$$\frac{\hat{\omega}_{\mathrm{m}}(s)}{\omega_{\mathrm{m}}(s)} = \frac{d_{\mathrm{c}}s + e_{\mathrm{c}}}{s^2 + d_{\mathrm{c}}s + e_{\mathrm{c}}} \tag{16}$$

With accurate model parameters, the estimation-error dynamics are locally stable in every operating point (marginally stable at zero speed). This observer design is a subset of all possible stable designs. However, it is easier to tune two second-order systems than one fourth-order system, which is a clear advantage of this gain selection.

III. Discrete-Time Model and Observer

Fig. 2 shows the framework of the discrete-time observer. Sampling of the stator currents is assumed to be synchronized with the pulse-width modulation (PWM). The switching-cycle averaged quantities are considered. Under these assumptions, the stator voltage in stator coordinates is piecewise constant between two consecutive sampling instants, which corresponds to the ZOH in stator coordinates. In other words, the stator voltage $\boldsymbol{u}_{\mathrm{s}}^{\mathrm{s}}(t)$ is constant during $kT_{\mathrm{s}} < t < (k+1)T_{\mathrm{s}}$, where T_{s} is the sampling period and k is the discrete-time index. Furthermore, the digital control system and PWM update have (at least) one-sampling-period time delay (the gray block z^{-1} in Fig. 2) due to the finite computation time. The effect of the time delay on the voltage angle is compensated for in the coordinate transformation of the reference voltage.

A. Exact Discrete Hold-Equivalent Model

The exact discrete-time state-space representation of (1) in rotor coordinates is given by

$$\boldsymbol{\psi}_{\mathrm{s}}^{\mathrm{r}}(k+1) = \boldsymbol{\Phi}\boldsymbol{\psi}_{\mathrm{s}}^{\mathrm{r}}(k) + \boldsymbol{\Gamma}\boldsymbol{u}_{\mathrm{s}}^{\mathrm{r}}(k) + \boldsymbol{\gamma}\psi_{\mathrm{pm}} \tag{17a}$$

$$\boldsymbol{i}_{\mathrm{s}}^{\mathrm{r}}(k) = \boldsymbol{C}\boldsymbol{\psi}_{\mathrm{s}}^{\mathrm{r}}(k) + \boldsymbol{d}\psi_{\mathrm{pm}} \tag{17b}$$

where the system matrices are [22]

$$\boldsymbol{\Phi} = \mathrm{e}^{\boldsymbol{A}T_{\mathrm{s}}} = \begin{bmatrix} \phi_{11} & -\phi_{21} \\ \phi_{21} & \phi_{22} \end{bmatrix}, \quad \boldsymbol{\gamma} = \int_0^{T_{\mathrm{s}}} \mathrm{e}^{\boldsymbol{A}\tau}\mathrm{d}\tau \cdot \boldsymbol{b} = \begin{bmatrix} \gamma_1 \\ \gamma_2 \end{bmatrix}$$

$$\boldsymbol{\Gamma} = \int_0^{T_{\mathrm{s}}} \mathrm{e}^{\boldsymbol{A}\tau}\mathrm{e}^{\omega_{\mathrm{m}}\tau\mathbf{J}}\mathrm{d}\tau \cdot \mathrm{e}^{-\omega_{\mathrm{m}}T_{\mathrm{s}}\mathbf{J}} = \begin{bmatrix} \gamma_{11} & \gamma_{12} \\ \gamma_{21} & \gamma_{22} \end{bmatrix} \tag{18}$$

In the above equation for $\boldsymbol{\Gamma}$, the ZOH of the stator voltage is modeled in stationary coordinates, where it physically is. Hence, the model inherently takes the ZOH delay properly into account. The closed-form expressions of the matrix elements are given in the Appendix. If the exact expressions are computationally too demanding, approximate expressions (series expansions) could be used instead.

B. Observer Structure

The discrete-time observer in estimated rotor coordinates is defined by

$$\hat{\boldsymbol{\psi}}_{\mathrm{s}}(k+1) = \hat{\boldsymbol{\Phi}}\hat{\boldsymbol{\psi}}_{\mathrm{s}}(k) + \hat{\boldsymbol{\Gamma}}\boldsymbol{u}_{\mathrm{s}}(k) + \hat{\boldsymbol{\gamma}}\psi_{\mathrm{pm}} + \boldsymbol{K}\tilde{\boldsymbol{i}}_{\mathrm{s}}(k) \tag{19a}$$

$$\hat{\boldsymbol{i}}_{\mathrm{s}}(k) = \boldsymbol{C}\hat{\boldsymbol{\psi}}_{\mathrm{s}}(k) + \boldsymbol{d}\psi_{\mathrm{pm}} \tag{19b}$$

where $\boldsymbol{K}$ is the gain matrix. It is worth noticing that the matrices $\hat{\boldsymbol{\Phi}}$, $\hat{\boldsymbol{\Gamma}}$, and $\hat{\boldsymbol{\gamma}}$ in the discrete-time observer are functions of the estimated speed $\hat{\omega}_{\mathrm{m}}$. This differs from the continuous-time case, where only the system matrix $\hat{\boldsymbol{A}}$ depends on the estimateed speed. As shown in Fig. 2, the effect of the computational delay on the stator voltage is compensated for by intentionally delaying the voltage input of the observer, i.e., $\boldsymbol{u}_{\mathrm{s}}(k) = \boldsymbol{u}_{\mathrm{s,ref}}(k-1)$. As mentioned before, the effect of the ZOH is inherently included in the exact discrete-time plant model. A discrete-time rotor-position estimation is

$$\hat{\vartheta}_{\mathrm{m}}(k+1) = \hat{\vartheta}_{\mathrm{m}}(k) + T_{\mathrm{s}}\hat{\omega}_{\mathrm{m}}(k) \tag{20}$$

and the speed-adaptation law is

$$\hat{\omega}_{\mathrm{i}}(k+1) = \hat{\omega}_{\mathrm{i}}(k) + T_{\mathrm{s}}\boldsymbol{k}_{\mathrm{i}}\tilde{\boldsymbol{i}}_{\mathrm{s}}(k) \tag{21a}$$

$$\hat{\omega}_{\mathrm{m}}(k) = \hat{\omega}_{\mathrm{i}}(k) + \boldsymbol{k}_{\mathrm{p}}\tilde{\boldsymbol{i}}_{\mathrm{s}}(k) \tag{21b}$$

where $\boldsymbol{k}_{\mathrm{p}} = [0, k_{\mathrm{p}}]$ and $\boldsymbol{k}_{\mathrm{i}} = [0, k_{\mathrm{i}}]$ are the gain vectors.

C. Estimation-Error Dynamics

1) Nonlinear Dynamics: For analyzing the estimation-error dynamics, the plant model (17) is transformed to estimated rotor coordinates as

$$\boldsymbol{\psi}_{\mathrm{s}}(k+1) = \boldsymbol{\Phi}'\boldsymbol{\psi}_{\mathrm{s}}(k) + \boldsymbol{\Gamma}'\boldsymbol{u}_{\mathrm{s}}(k) + \boldsymbol{\gamma}'\psi_{\mathrm{pm}} \tag{22a}$$

$$\boldsymbol{i}_{\mathrm{s}}(k) = \boldsymbol{C}'\boldsymbol{\psi}_{\mathrm{s}}(k) + \boldsymbol{d}'\psi_{\mathrm{pm}} \tag{22b}$$

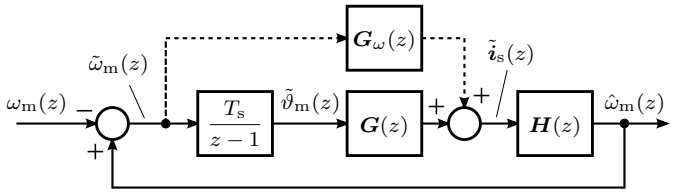

Fig. 3. Linearized estimation-error dynamics for the discrete-time observer design. The transfer-function matrix from $\tilde{\omega}_\mathrm{m}(z)$ to $\tilde{\boldsymbol{i}}_\mathrm{s}(z)$ is $\boldsymbol{G}_\omega(z) = \boldsymbol{C}(z\mathbf{I} - \boldsymbol{A}_\psi)^{-1}\boldsymbol{b}_\omega$. The dashed line disappears if $\boldsymbol{b}_\omega = \mathbf{0}$ is assumed.

where

$$\begin{aligned}\boldsymbol{\Phi}' &= \mathrm{e}^{-\tilde{\vartheta}_\mathrm{m}(k+1)\mathbf{J}}\boldsymbol{\Phi}\mathrm{e}^{\tilde{\vartheta}_\mathrm{m}(k)\mathbf{J}}\\ \boldsymbol{\Gamma}' &= \mathrm{e}^{-\tilde{\vartheta}_\mathrm{m}(k+1)\mathbf{J}}\boldsymbol{\Gamma}\mathrm{e}^{\tilde{\vartheta}_\mathrm{m}(k)\mathbf{J}}, \quad \boldsymbol{\gamma}' = \mathrm{e}^{-\tilde{\vartheta}_\mathrm{m}(k+1)\mathbf{J}}\boldsymbol{\gamma}\\ \boldsymbol{C}' &= \mathrm{e}^{-\tilde{\vartheta}_\mathrm{m}(k)\mathbf{J}}\boldsymbol{C}\mathrm{e}^{\tilde{\vartheta}_\mathrm{m}(k)\mathbf{J}}, \quad \boldsymbol{d}' = \mathrm{e}^{-\tilde{\vartheta}_\mathrm{m}(k)\mathbf{J}}\boldsymbol{d}\end{aligned} \tag{23}$$

The nonlinear estimation-error dynamics become

$$\begin{aligned}\tilde{\boldsymbol{\psi}}_\mathrm{s}(k+1) &= (\hat{\boldsymbol{\Phi}} + \boldsymbol{K}\boldsymbol{C})\tilde{\boldsymbol{\psi}}_\mathrm{s}(k) + (\tilde{\boldsymbol{\Phi}} + \boldsymbol{K}\tilde{\boldsymbol{C}})\boldsymbol{\psi}_\mathrm{s}(k)\\ &\quad + (\tilde{\boldsymbol{\gamma}} + \boldsymbol{K}\tilde{\boldsymbol{d}})\psi_\mathrm{pm} + \tilde{\boldsymbol{\Gamma}}\boldsymbol{u}_\mathrm{s}(k) \qquad (24a)\\ \tilde{\boldsymbol{i}}_\mathrm{s}(k) &= \boldsymbol{C}\tilde{\boldsymbol{\psi}}_\mathrm{s}(k) + \tilde{\boldsymbol{d}}\psi_\mathrm{pm} + \tilde{\boldsymbol{C}}\boldsymbol{\psi}_\mathrm{s}(k) \qquad (24b)\end{aligned}$$

where $\tilde{\boldsymbol{\Phi}} = \hat{\boldsymbol{\Phi}} - \boldsymbol{\Phi}'$ and other matrices are defined similarly.

2) Linearized Dynamics: Linearization of (24) leads to

$$\tilde{\boldsymbol{\psi}}_\mathrm{s}(k+1) = \boldsymbol{A}_\psi\tilde{\boldsymbol{\psi}}_\mathrm{s}(k) + \boldsymbol{b}_\vartheta\tilde{\vartheta}_\mathrm{m}(k) + \boldsymbol{b}_\omega\tilde{\omega}_\mathrm{m}(k) \tag{25a}$$

$$\tilde{\boldsymbol{i}}_\mathrm{s}(k) = \boldsymbol{C}\tilde{\boldsymbol{\psi}}_\mathrm{s}(k) + \boldsymbol{d}_\vartheta\tilde{\vartheta}_\mathrm{m}(k) \tag{25b}$$

where the system matrices are

$$\begin{aligned}\boldsymbol{A}_\psi &= \boldsymbol{\Phi}_0 + \boldsymbol{K}\boldsymbol{C}, \quad \boldsymbol{d}_\vartheta = (\mathbf{J}\boldsymbol{C} - \boldsymbol{C}\mathbf{J})\,\boldsymbol{\psi}_{\mathrm{s}0} + \mathbf{J}\boldsymbol{d}\psi_\mathrm{pm}\\ \boldsymbol{b}_\omega &= \left(\frac{\partial\boldsymbol{\Phi}_0}{\partial\omega_\mathrm{m}}\bigg|_0 + T_\mathrm{s}\mathbf{J}\boldsymbol{\Phi}\right)\boldsymbol{\psi}_{\mathrm{s}0} + \left(\frac{\partial\boldsymbol{\gamma}}{\partial\omega_\mathrm{m}}\bigg|_0 + T_\mathrm{s}\mathbf{J}\boldsymbol{\gamma}_0\right)\psi_\mathrm{pm}\\ &\quad + \left(\frac{\partial\boldsymbol{\Gamma}}{\partial\omega_\mathrm{m}}\bigg|_0 + T_\mathrm{s}\mathbf{J}\boldsymbol{\Gamma}_0\right)\boldsymbol{u}_{\mathrm{s}0}\\ \boldsymbol{b}_\vartheta &= (\mathbf{J}\boldsymbol{\Phi}_0 - \boldsymbol{\Phi}_0\mathbf{J})\boldsymbol{\psi}_{\mathrm{s}0} + \mathbf{J}\boldsymbol{\gamma}_0\psi_\mathrm{pm} + \boldsymbol{K}\boldsymbol{d}_\vartheta\\ &\quad + (\mathbf{J}\boldsymbol{\Gamma}_0 - \boldsymbol{\Gamma}_0\mathbf{J})\,\boldsymbol{u}_{\mathrm{s}0}\end{aligned} \tag{26}$$

The elements of $\boldsymbol{b}_\omega$ approach zero as the sampling period T_s approaches zero.[1] The corresponding transfer-function matrix from $\tilde{\vartheta}_\mathrm{m}(z)$ to $\tilde{\boldsymbol{i}}_\mathrm{s}(z)$ is

$$\boldsymbol{G}(z) = \boldsymbol{C}(z\mathbf{I} - \boldsymbol{A}_\psi)^{-1}\boldsymbol{b}_\vartheta + \boldsymbol{d}_\vartheta \tag{27}$$

The transfer-function matrix from $\tilde{\boldsymbol{i}}_\mathrm{s}(z)$ to $\hat{\omega}_\mathrm{m}(z)$, corresponding to the adaptation law (21), is $\boldsymbol{H}(z) = \boldsymbol{k}_\mathrm{p} + T_\mathrm{s}\boldsymbol{k}_\mathrm{i}/(z-1)$. Fig. 3 presents the block diagram of the linearized estimation-error dynamics.

D. Gain Selection

The linearized system in Fig. 3 is of the fourth order, and in general, explicit expressions for the gain selection might not exist. In order to obtain an approximate solution, $\boldsymbol{b}_\omega = \mathbf{0}$ is assumed. Further, $\boldsymbol{b}_\vartheta = \mathbf{0}$ can be forced if the observer gain

$$\boldsymbol{K} = \begin{bmatrix} L_\mathrm{d}k_1 & L_\mathrm{q}(v - \beta k_1)\\ L_\mathrm{d}k_2 & L_\mathrm{q}(w - \beta k_2)\end{bmatrix} \tag{28}$$

with

$$\begin{aligned}v &= \big[u_\mathrm{q}(\gamma_{11} - \gamma_{22}) - u_\mathrm{d}(\gamma_{12} + \gamma_{21})\\ &\quad + (\phi_{11} - \phi_{22})\hat{\psi}_\mathrm{q} - \gamma_2\psi_\mathrm{pm}\big]/\psi_\mathrm{f} \qquad (29a)\\ w &= \big[u_\mathrm{d}(\gamma_{11} - \gamma_{22}) + u_\mathrm{q}(\gamma_{12} + \gamma_{21})\\ &\quad + (\phi_{11} - \phi_{22})\hat{\psi}_\mathrm{d} + \gamma_1\psi_\mathrm{pm}\big]/\psi_\mathrm{f} \qquad (29b)\end{aligned}$$

is selected. This design principle is analogous to the continuous-time case presented in Section II-D.

The fourth-order characteristic polynomial is expressed as a product of two second-order polynomials $(z^2 + bz + c)(z^2 + dz + e)$, where the first part corresponds to the flux estimation and the second part corresponds to the speed adaptation. The resulting stabilizing gain selection is

$$\begin{aligned}k_1 &= -\big[(\phi_{11}^2 + b\phi_{11} - \phi_{21}^2 + \phi_{21}v + c)\beta\\ &\quad + (\phi_{11} + \phi_{22} + b + w)(v - \phi_{21})\big]/D \qquad (30a)\\ k_2 &= \big[\phi_{21}^2 - \phi_{21}v - c - (\phi_{22} + w)(\phi_{22} + b + w)\\ &\quad - (\phi_{11} + \phi_{22} + b + w)\phi_{21}\beta\big]/D \qquad (30b)\end{aligned}$$

where $D = v - \phi_{21}(1 + \beta^2) + (\phi_{11} - \phi_{22} - w)\beta$. It is to be noted that as the speed approaches zero, the gains k_1 and k_2 approach the following values:

$$k_1 = \frac{\phi_{11}^2 + b\phi_{11} + c}{\phi_{22} - \phi_{11}}, \quad k_2 = 0 \tag{31}$$

The speed-adaptation gains are

$$k_\mathrm{p} = \frac{L_\mathrm{q}(d+2)}{T_\mathrm{s}\psi_\mathrm{f}}, \quad k_\mathrm{i} = \frac{L_\mathrm{q}(d+e+1)}{T_\mathrm{s}^2\psi_\mathrm{f}} \tag{32}$$

IV. Experimental Setup and Parameters

A 6.7-kW four-pole SyRM drive is considered. The rated values are: speed 3175 r/min; frequency 105.8 Hz; line-to-line rms voltage 370 V; rms current 15.5 A; and torque 20.1 Nm. The total moment of inertia is 0.015 kgm^2 (2.7 times the inertia of the SyRM rotor). The control system was implemented in a dSPACE DS1104 PPC/DSP board. The SyRM is fed by a frequency converter that is controlled by the DS1104 board. The stator currents and the DC-link voltage are measured. A simple current feedforward compensation for dead times and power device voltage drops is applied. The magnetic saturation of the SyRM is modeled according to [23], but the incremental inductances are omitted for simplicity. A servo motor was used as a loading machine. The actual rotor speed ω_m and position ϑ_m are measured using an incremental encoder for monitoring purposes.

The current controller designed in the discrete-time domain is used [22]. The current-controller bandwidth is 1 p.u. It is worth noticing that the performance and the stability of the control system would be significantly deteriorated,

[1]For example, with 1-kHz sampling frequency $\boldsymbol{b}_\omega \approx [0.004, 0.016]^\mathrm{T}$ p.u. at the rated speed for the studied motor.

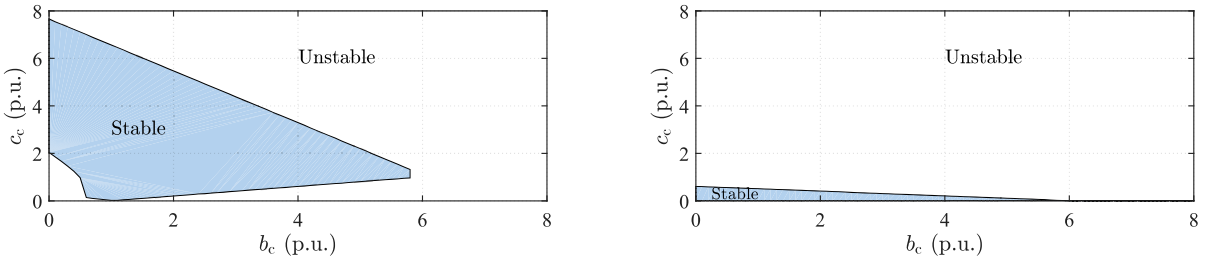

Fig. 4. Areas of stable operation in space of design parameters b_c and c_c when the continuous-time design with the forward Euler approximation is used: (a) ω_m = 1 p.u. and (b) ω_m = 0.1 p.u. Accurate parameter estimates are assumed. The sampling frequency is 2 kHz.

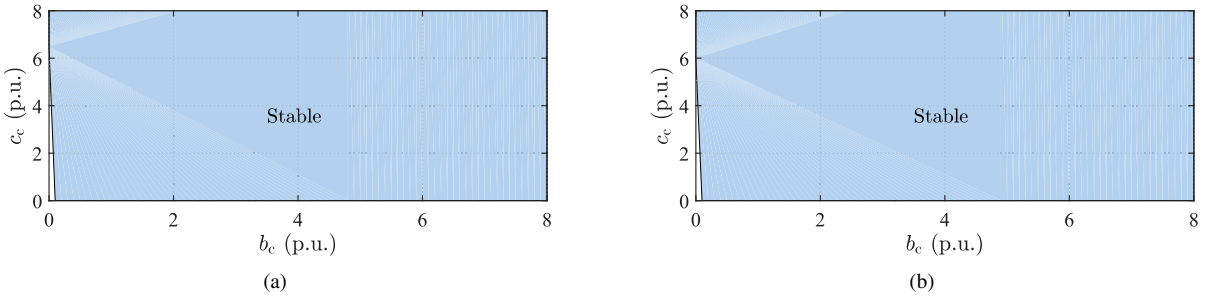

Fig. 5. Areas of stable operation in space of design parameters b_c and c_c when the direct discrete-time design is used: (a) ω_m = 1 p.u. and (b) ω_m = 0.1 p.u. Accurate parameter estimates are assumed. The sampling frequency is 1 kHz. Small unstable areas (not shaded) near $b_c = 0$ can be observed.

if the current controller were designed in the continuous-time domain and then discretized, e.g., by using the forward Euler approximation. The control system shown in Fig. 2 is augmented with a 2DOF PI-type speed controller, including active damping, whose feedback signal is the speed estimate $\hat{\omega}_m$ obtained from the observer. The approximate bandwidth of the speed-control loop was 0.01 p.u.

The discrete-time flux observer (19) with the speed adaptation law (21) has been implemented using the proposed gain selections (28) and (32). The selection of b_c and c_c is similar to the one proposed in [14]:

$$b_c = 0.1 + 0.75|\hat{\omega}_m|, \quad c_c = 1.5 b_c |\hat{\omega}_m| \tag{33}$$

where per-unit values are used. The poles of the speed-adaptation loop are placed according to the characteristic equation $s^2 + 2\xi\rho + \rho^2$, where $\rho = 0.8$ p.u. and $\xi = 1$, i.e., $d_c = 2\rho$ and $e_c = \rho^2$. The continuous-time parameters b_c and c_c are mapped to their discrete-time equivalents as

$$b = -2\mathrm{e}^{-b_c T_s/2} \cosh\left(T_s \sqrt{c_c - b_c^2/4}\right), \quad c = \mathrm{e}^{-b_c T_s} \tag{34}$$

The parameters d and e are obtained from d_c and e_c in a similar manner.

V. Results

The motion-sensorless control system with the discrete-time observer design is evaluated by means of the stability analysis, simulations, and experiments. The stability analysis and simulation results corresponding to the continuous-time design with the forward Euler discretization are also presented for comparison.

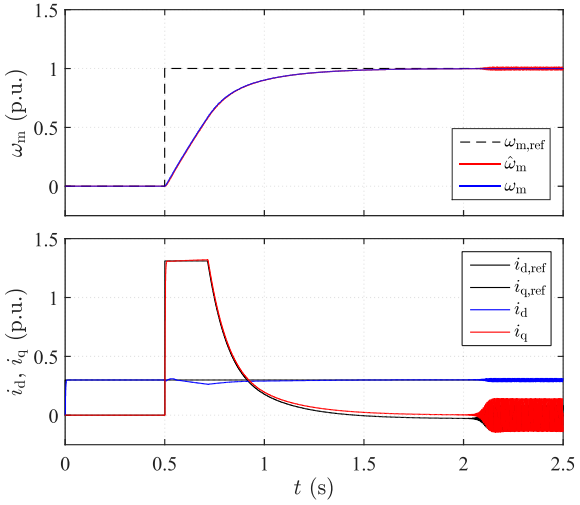

Fig. 6. Simulation results for the continuous-time observer design, which is discretized using the forward Euler approximation. The speed reference is stepped from zero to the rated speed. The sampling frequency is 4 kHz and ρ = 0.8 p.u. The first subplot shows the reference speed $\omega_{m,ref}$, the actual speed ω_m, and the estimated speed $\hat{\omega}_m$. The second subplot shows the currents i_d and i_q.

A. Stability Analysis

The stability of the estimation-error dynamics is evaluated in the space of design parameters b_c and c_c. The operating-point current components are $i_d = 0.3$ p.u. and $i_q = 0$. The actual parameters are: $R_s = 0.047$ p.u., $L_d = 2.0$ p.u., and $L_q = 0.3$ p.u.

The stability of the continuous-time design with the for-

ward Euler discretization and accurate parameter estimates is illustrated in Fig. 4 at two different speeds. The speeds are 1 p.u. and 0.1 p.u. in Figs. 4(a) and 4(b), respectively. The sampling frequency is 2 kHz. It can be seen that even with the accurate parameter estimates the stable area is very small at low speeds. The stable area at the rated speed is larger, but yet shrinks rapidly as b_c increases. There is more freedom to select c_c when b_c is small, but choosing b_c to be small may result in poorly damped flux-estimation dynamics. When the parameter errors and the current control loop are taken into account, the stable area vanishes quickly, suggesting that it would be difficult to start the motor if the sampling frequency is low.

For comparison, similar stability maps for the iscrete-time design are shown in Fig. 5, where the sampling frequency is 1 kHz. Fig. 5 shows that the stability of the discrete-time design is practically independent of the speed. Almost the entire area where $b_\mathrm{c} > 0$ and $c_\mathrm{c} > 0$ is stable, as it ideally should be. The small unstable areas near $b_\mathrm{c} = 0$ originate from nonzero $\boldsymbol{b}_\omega$, which is omitted in the gain selection.

B. Simulations

First, the continuous-time observer design, discretized using the forward Euler approximation, is considered. The sampling frequency is 4 kHz. An example of simulation results is shown in Fig. 6. The motor is accelerated from zero to the rated speed, while the d-axis current reference $i_{\mathrm{d,ref}} = 0.3$ p.u. and the q-axis current reference $i_{\mathrm{q,ref}}$ is determined by the speed controller. It can be seen that there are large oscillations in the speed estimate. If the sampling frequency were decreased further the system would become unstable.

Next, the proposed discrete-time design is studied. An example of simulation results at the sampling frequency of 2 kHz is shown in Fig. 7. It can be seen that the estimated speed $\hat{\omega}_\mathrm{m}$ follows the actual speed ω_m nicely and there is no visible difference between them. In Fig. 7(b), the load torque step of 75% of the rated is applied at $t = 0.5$ s. It can be seen that the observer behaves well and the speed estimate is following the actual speed nicely. With the discrete-time design, the sampling frequency could be lowered even below 0.3 kHz in the ideal case.

C. Experiments

The proposed discrete-time observer design is experimentally evaluated at the sampling frequency of 2 kHz. Fig. 8 shows experimental results corresponding to the simulation case. It can be seen that the estimated speed $\hat{\omega}_\mathrm{m}$ follows the actual speed ω_m without any large variations. It is to be noted that $\hat{\omega}_\mathrm{m}$ comes directly from (21) without low-pass filtering.

Compared to the simulation results, there is much more noise in the waveforms of i_d and i_q. This noise consists mainly of low-order (sixth and lower orders) harmonics. After the load torque step, the dominant harmonic component in i_q is of the sixth order, having the peak value of about 0.03 p.u. These low-order harmonics originate mainly from the nonsinusoidal spatial distribution of the stator inductance [24] and the magnetic saturation characteristics of the prototype SyRM used in the experiments. However, despite these harmonics, the observer works well.

VI. Conclusions

A speed-adaptive full-order observer for motion-sensorless IPMSM and SyRM drives was designed directly in the discrete-time domain. The hold-equivalent model applied in the design can be either the exact model or a series expansion. The effects of the ZOH and time delays are inherently taken into account in the design. The closed-loop estimation-error dynamics were linearized and the stabilizing gains were derived using the resulting small-signal model. The stability of the proposed discrete-time design was compared with the continuous-time design using eigenvalue analysis, simulations, and experiments. Based on the results, performance improvements obtained via the direct discrete-time design—compared to the corresponding continuous-time designs—indicate drastic performance improvements, if the ratio between the sampling frequency and the fundamental frequency is low.

Appendix
Exact Discrete-Time Model

In the derivation of the model [22], the rotor speed and the motor parameters have been assumed to be constant during the sampling period. The closed-form solutions for the elements of $\boldsymbol{\Phi}$ in (18) are

$$\begin{aligned}
\phi_{11} &= \mathrm{e}^{-\sigma T_\mathrm{s}}\left[\cosh(\lambda T_\mathrm{s}) - \delta\frac{\sinh(\lambda T_\mathrm{s})}{\lambda}\right] \\
\phi_{22} &= \mathrm{e}^{-\sigma T_\mathrm{s}}\left[\cosh(\lambda T_\mathrm{s}) + \delta\frac{\sinh(\lambda T_\mathrm{s})}{\lambda}\right] \\
\phi_{21} &= -\omega_\mathrm{m}\mathrm{e}^{-\sigma T_\mathrm{s}}\frac{\sinh(\lambda T_\mathrm{s})}{\lambda}
\end{aligned} \tag{35}$$

where $\lambda = \sqrt{\delta^2 - \omega_\mathrm{m}^2}$ and[2]

$$\sigma = \frac{R_\mathrm{s}}{2}\left(\frac{1}{L_\mathrm{d}} + \frac{1}{L_\mathrm{q}}\right), \quad \delta = \frac{R_\mathrm{s}}{2}\left(\frac{1}{L_\mathrm{d}} - \frac{1}{L_\mathrm{q}}\right) \tag{36}$$

The closed-form solutions for the elements of $\boldsymbol{\Gamma}$ in (18) are

$$\begin{aligned}
\gamma_{11} &= G\Big[g_{11}\cos(\omega_\mathrm{m}T_\mathrm{s}) - g_{12}\sin(\omega_\mathrm{m}T_\mathrm{s}) - g_{11}\phi_{11} \\
&\qquad + (\sigma+\delta)\omega_\mathrm{m}^2(\phi_{11} - \phi_{22})\Big] \\
\gamma_{12} &= G\Big[g_{12}\cos(\omega_\mathrm{m}T_\mathrm{s}) + g_{11}\sin(\omega_\mathrm{m}T_\mathrm{s}) - g_{12}\phi_{11} + g_{22}\phi_{21}\Big] \\
\gamma_{21} &= G\Big[g_{21}\cos(\omega_\mathrm{m}T_\mathrm{s}) - g_{22}\sin(\omega_\mathrm{m}T_\mathrm{s}) - g_{21}\phi_{22} - g_{11}\phi_{21}\Big] \\
\gamma_{22} &= G\Big[g_{22}\cos(\omega_\mathrm{m}T_\mathrm{s}) + g_{21}\sin(\omega_\mathrm{m}T_\mathrm{s}) - g_{22}\phi_{22} \\
&\qquad + (\sigma-\delta)\omega_\mathrm{m}^2(\phi_{22} - \phi_{11})\Big]
\end{aligned} \tag{37}$$

[2]If $\omega_\mathrm{m}^2 > \delta^2$, then $\lambda = \mathrm{j}\lambda_\mathrm{im} = \mathrm{j}\sqrt{\omega_\mathrm{m}^2 - \delta^2}$ is imaginary. All the matrix elements remain real since $\cosh(\mathrm{j}\lambda_\mathrm{im}T_\mathrm{s}) = \cos(\lambda_\mathrm{im}T_\mathrm{s})$ and $\sinh(\mathrm{j}\lambda_\mathrm{im}T_\mathrm{s})/(\mathrm{j}\lambda_\mathrm{im}) = \sin(\lambda_\mathrm{im}T_\mathrm{s})/\lambda_\mathrm{im}$ hold due to the properties of hyperbolic functions. Furthermore, for $\lambda = 0$, these functions reduce to $\cosh(\lambda T_\mathrm{s}) = \sinh(\lambda T_\mathrm{s})/\lambda = 1$.

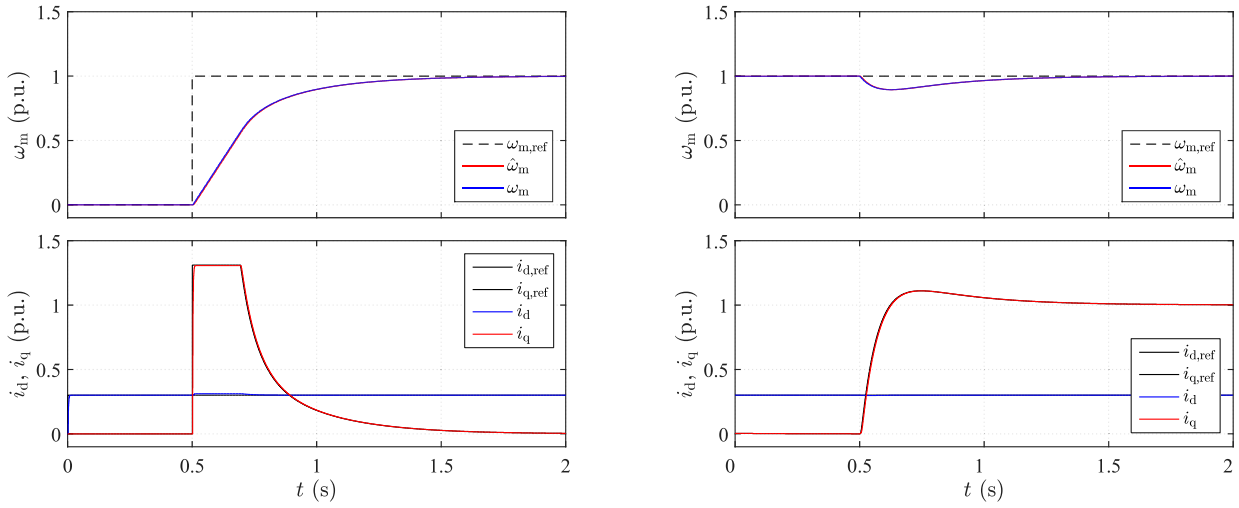

(a) (b)

Fig. 7. Simulation results for the discrete-time design: (a) speed reference is stepped from zero to the rated speed; (b) torque step is applied at the rated speed. The sampling frequency is 2 kHz.

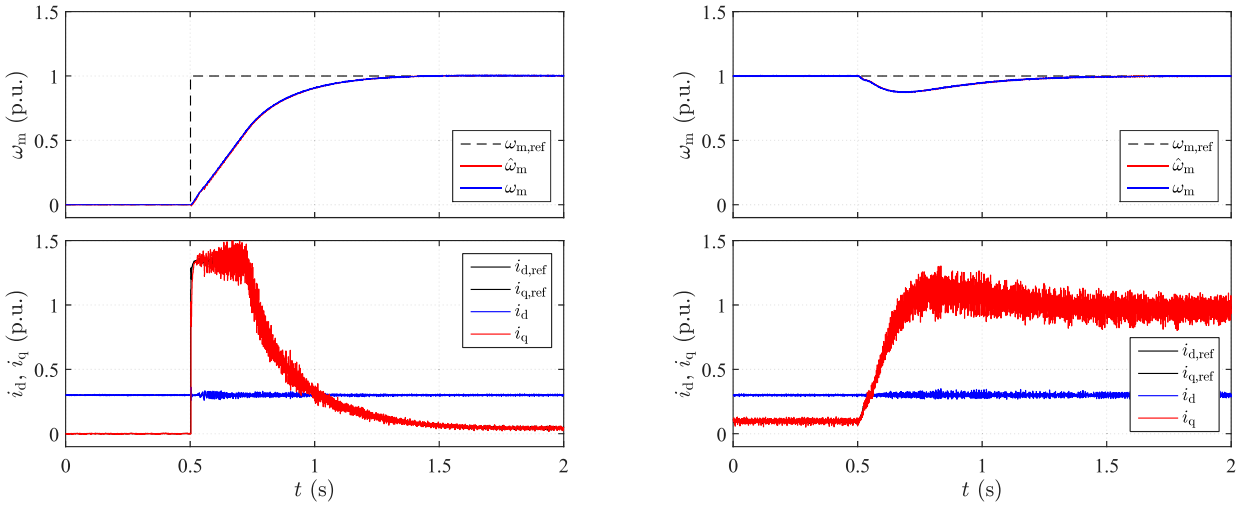

(a) (b)

Fig. 8. Experimental results for the discrete-time design: (a) speed reference is stepped from zero to the rated speed; (b) torque step is applied at the rated speed. The sampling frequency is 2 kHz.

where $G = 1/[(\sigma^2 - \delta^2)^2 + 4\sigma^2\omega_{\mathrm{m}}^2]$ and

$$g_{11} = (\sigma - \delta)^2(\sigma + \delta) + 4\sigma\omega_{\mathrm{m}}^2, \quad g_{12} = 2(\sigma - \delta)\delta\omega_{\mathrm{m}}$$
$$g_{21} = 2(\sigma + \delta)\delta\omega_{\mathrm{m}}, \quad g_{22} = (\sigma + \delta)^2(\sigma - \delta) + 4\sigma\omega_{\mathrm{m}}^2 \quad (38)$$

In the previous derivations, it is important to notice that $\mathrm{e}^{x+y} = \mathrm{e}^x\mathrm{e}^y$ does not hold for matrix exponentials in general. The elements of $\boldsymbol{\gamma}$ in (18) are given by

$$\gamma_1 = H\left[(\sigma - \delta)(1 - \phi_{11}) - \omega_{\mathrm{m}}\phi_{21}\right]$$
$$\gamma_2 = H\left[-\sigma\phi_{21} + \omega_{\mathrm{m}}\left(\frac{\phi_{11} + \phi_{22}}{2} - 1\right)\right] \quad (39)$$

where $H = (\sigma + \delta)/[(\sigma + \delta)(\sigma - \delta) + \omega_{\mathrm{m}}^2]$.

ACKNOWLEDGMENT

The work was supported in part by ABB Oy and in part by the Academy of Finland.

REFERENCES

[1] G. Pellegrino, A. Vagati, P. Guglielmi, and B. Boazzo, "Performance comparison between surface-mounted and interior PM motor drives for electric vehicle application," *IEEE Trans. Ind. Electron.*, vol. 59, no. 2, pp. 803–811, Feb. 2012.

[2] J.-I. Ha, S.-J. Kang, and S.-K. Sul, "Position-controlled synchronous reluctance motor without rotational transducer," *IEEE Trans. Ind. Appl.*, vol. 35, no. 6, pp. 1393–1398, Nov./Dec. 1999.

[3] E. Capecchi, P. Guglielmo, M. Pastorelli, and A. Vagati, "Position-sensorless control of the transverse-laminated synchronous reluctance motor," *IEEE Trans. Ind. Appl.*, vol. 37, no. 6, pp. 1768–1776, Nov./Dec. 2001.

[4] H. F. Hofmann, S. R. Sanders, and A. EL-Antably, "Stator-flux-oriented vector control of synchronous reluctance machines with maximized efficiency," *IEEE Trans. Ind. Electron.*, vol. 51, no. 5, pp. 1066–1072, Oct. 2004.

[5] S. Koonlaboon and S. Sangwongwanich, "Sensorless control of interior permanent-magnet synchronous motors based on a fictitious permanent-magnet flux model," in *Conf. Rec. IEEE-IAS Annu. Meeting*, Hong Kong, Oct. 2005, pp. 1111–1118.

[6] A. Consoli, G. Scarcella, G. Scelba, A. Testa, and D. A. Triolo, "Sensorless rotor position estimation in synchronous reluctance motors exploiting a flux deviation approach," *IEEE Trans. Ind. Appl.*, vol. 43, no. 5, pp. 1266–1273, Sep./Oct. 2007.

[7] R. Morales-Caporal and M. Pacas, "Encoderless predictive direct torque control for synchronous reluctance machines at very low and zero speed," *IEEE Trans. Ind. Electron.*, vol. 55, no. 12, pp. 4408–4416, Dec. 2008.

[8] A. Piippo, M. Hinkkanen, and J. Luomi, "Analysis of an adaptive observer for sensorless control of interior permanent magnet synchronous motors," *IEEE Trans. Ind. Electron.*, vol. 55, no. 2, pp. 570–576, Feb. 2008.

[9] ——, "Adaptation of motor parameters in sensorless PMSM drives," *IEEE Trans. Ind. Appl.*, vol. 45, no. 1, pp. 203–212, Jan./Feb. 2009.

[10] P. Landsmann, R. Kennel, H. de Kock, and M. Kamper, "Fundamental saliency based encoderless control for reluctance synchronous machines," in *Proc. ICEM'10*, Rome, Italy, Sept. 2010.

[11] A. Ghaderi and T. Hanamoto, "Wide-speed-range sensorless vector control of synchronous reluctance motors based on extended programmable cascaded low-pass filters," *IEEE Trans. Ind. Electron.*, vol. 58, no. 6, pp. 2322–2333, June 2011.

[12] K. Kato, M. Tomita, M. Hasegawa, S. Doki, S. Okuma, and S. Kato, "Position and velocity sensorless control of synchronous reluctance motor at low speed using disturbance observer for high-frequency extended EMF," in *Proc. IEEE IECON'11*, vol. 1, Melbourne, Australia, Nov. 2011, pp. 1971–1976.

[13] S.-C. Agarlită, I. Boldea, and F. Blaabjerg, "High-frequency-injection-assisted "active flux"-based sensorless vector control of reluctance synchronous motors, with experiments from zero speed," *IEEE Trans. Ind. Appl.*, vol. 48, no. 6, pp. 1931–1939, Nov./Dec. 2012.

[14] T. Tuovinen, M. Hinkkanen, L. Harnefors, and J. Luomi, "Comparison of a reduced-order observer and a full-order observer for sensorless synchronous motor drives," *IEEE Trans. Ind. Appl.*, vol. 48, no. 6, pp. 1959–1967, Nov./Dec. 2012.

[15] M.-Y. Wei and T.-H. Liu, "Design and implementation of an online tuning adaptive controller for synchronous reluctance motor drives," *IEEE Trans. Ind. Electron.*, vol. 60, no. 9, pp. 3644–3657, Sep. 2013.

[16] W. Xu and R. D. Lorenz, "High-frequency injection-based stator flux linkage and torque estimation for DB-DTFC implementation on IPMSMs considering cross-saturation effects," *IEEE Trans. Ind. Appl.*, vol. 50, no. 6, pp. 3805–3815, Nov. 2014.

[17] K.-K. Huh and R. D. Lorenz, "Discrete-time domain modeling and design for AC machine current regulation," in *Conf. Rec. IEEE-IAS Annu. Meeting*, New Orleans, LA, Sept. 2007, pp. 2066–2073.

[18] H. Kim, M. W. Degner, J. M. Guerrero, F. Briz, and R. D. Lorenz, "Discrete-time current regulator design for AC machine drives," *IEEE Trans. Ind. Appl.*, vol. 46, no. 4, pp. 1425–1435, July/Aug. 2010.

[19] W. Peters, T. Huber, and J. Böcker, "Control realization for an interior permanent magnet synchronous motor (IPMSM) in automotive drive trains," in *Conf. PCIM 2011*, vol. 1, Nuremberg, Germany, May 2011, pp. 98–103.

[20] W. Peters and J. Böcker, "Discrete-time design of adaptive current controller for interior permanent magnet synchronous motors (IPMSM) with high magnetic saturation," in *Proc. IEEE IECON'13*, Vienna, Austria, Nov. 2013, pp. 6608–6613.

[21] J. S. Lee, C.-H. Choi, J.-K. Seok, and R. D. Lorenz, "Deadbeat-direct torque and flux control of interior permanent magnet synchronous machines with discrete time stator current and stator flux linkage observer," *IEEE Trans. Ind. Appl.*, vol. 47, no. 4, pp. 1749–1758, July/Aug. 2011.

[22] M. Hinkkanen, Z. Qu, H. A. A. Awan, T. Tuovinen, and F. Briz, "Current control for IPMSM drives: direct discrete-time pole-placement design," in *Proc. IEEE WEMDCD'2015*, Torino, Italy, Mar. 2015.

[23] Z. Qu, T. Tuovinen, and M. Hinkkanen, "Inclusion of magnetic saturation in dynamic models of synchronous reluctance motors," in *Proc. ICEM'12*, Marseille, France, Sept. 2012, pp. 994–1000.

[24] A. Piippo and J. Luomi, "Torque ripple reduction in sensorless PMSM drives," in *Proc. IEEE IECON'06*, Paris, France, Nov. 2006, pp. 920–925.